# Self-Assembly of a Donor–Acceptor Dyad Across Multiple Length Scales: Functional Architectures for Organic Electronics

**ARTICLE** *in* ADVANCED FUNCTIONAL MATERIALS · AUGUST 2009

Impact Factor: 11.81 · DOI: 10.1002/adfm.200900366

FULL PAPER

# Self-Assembly of a Donor-Acceptor Dyad Across Multiple Length Scales: Functional Architectures for Organic Electronics

By *Jeffrey M. Mativetsky, Marcel Kastler, Rebecca C. Savage, Desirée Gentilini, Matteo Palma, Wojciech Pisula, Klaus Müllen,** and *Paolo Samorì**

**Molecular dyads based on polycyclic electron donor (D) and electron acceptor (A) units represent suitable building blocks for forming highly ordered, solution-processable, nanosegregated D-A domains for potential use in (opto)electronic applications. A new dyad, based on alkyl substituted hexa-*peri*-hexabenzocoronene (HBC) and perylene monoimide (PMI) separated by an ethinylene linker, is shown to have a high tendency to self-assemble into ordered supramolecular arrangements at multiple length scales: macroscopic extruded filaments display long-range crystalline order, nanofiber networks are produced by simple spin-coating, and monolayers with a lamellar packing are formed by physisorption at the solution-HOPG interface. Moreover, highly uniform mesoscopic ribbons bearing atomically flat facets and steps with single-molecule heights self-assemble upon solvent-vapor annealing. Electrical measurements of HBC-PMI films and mesoscopic ribbons in a transistor configuration exhibit ambipolar transport with well balanced p- and n-type mobilities. Owing to the increased level of order at the supramolecular level, devices based on ribbons show mobility increases of more than one order of magnitude.**

## 1. Introduction

It is well established that the properties and performance of organic (opto)electronic devices strongly depend on the degree of supramolecular order within the active layers.[1–12] Nevertheless, solution processing, which is desirable for the development of low-cost organic devices, often leads to disordered materials. Functional molecular systems which can self-assemble into ordered architectures are thus key to the development of solution-based organic electronics. The mediation of intermolecular interactions through non-covalent forces such as hydrogen-bonds and π-π stacking is highly sought after as an approach to improving supramolecular order in materials for organic devices.[13] In particular, systems featuring extended π-conjugation and π-stacking are relevant for electrical applications owing to their delocalized electronic structure and potential high degree of order.[14–22]

Molecules with electron donor (D) and electron acceptor (A) functionalities have recently attracted a great deal of attention because of their potential application in artificial photosynthesis[23] and organic solar cells.[24–27] An increasingly common and successful approach to organic photovoltaics is based on bulk heterojunctions, i.e. interpenetrating blends of D and A components.[24–26] Blends of D and A components have also been exploited for producing ambipolar, i.e. both p-type and n-type, transport characteristics.[28] Organic molecules, while generally expected to be both electron and hole conductors, typically exhibit only unipolar behavior. It is thought that this arises from the trapping of charge at the molecule-dielectric interface or by large charge injection barriers at the molecule-electrode interface.[29] Ambipolar transport is of interest for producing ambipolar organic field effect transistors (OFETs)[28–35] and organic light emitting field-effect transistors (OLETs).[33,36–38] Ambipolar OFETs, which could form the basis of organic complementary metal oxide semiconductor (CMOS) logic circuits,[28,32,39,40] would enable the development of robust, low-noise, low-power organic electronics. OLETs, which combine the switching functionality of a transistor with light emission due to charge recombination, are seen as having advantages over organic light emitting diodes (OLEDs) and a large potential for applications such as display technologies.[37,38]

Given their excellent self-assembly and electronic properties, synthetic nanographenes,[5,21,41–43] such as hexa-*peri*-hexabenzocoronene (HBC), and perylene dyes,[15,44–54] including perylene diimide (PDI) and perylene monoimide (PMI), are highly promising for applications in organic electronic devices.

[*] Prof. K. Müllen, Dr. M. Kastler, Dr. W. Pisula[+]
Max Planck Institute for Polymer Research
Ackermannweg 10, 55128 Mainz (Germany)
E-mail: muellen@mpip-mainz.mpg.de
Prof. P. Samorì, Dr. J. M. Mativetsky, R. C. Savage, D. Gentilini, Dr. M. Palma
Institut de Science et d'Ingénierie Supramoléculaires (ISIS)
CNRS 7006
Université de Strasbourg
8, allée Gaspard Monge, 67000 Strasbourg (France)
E-mail: samori@isis-ulp.org
[+] Present address: Evonik Degussa GmbH Process Technology & Engineering Process Technology—New Processes, Rodenbacher Chaussee 4, 63457 Hanau-Wolfgang (Germany)

DOI: 10.1002/adfm.200900366

Moreover, blends of these materials, with the HBC acting as a D component and PDI acting as an A component, have already been successfully employed in organic photovoltaic devices with high external quantum efficiencies.[26] It was shown that the good performance was largely due to a phase-segregated structure which provided a large interfacial area between the D and A parts. In an effort to produce D-A systems featuring phase separation at the nanometer scale, and as an alternative strategy to blending,[28] which generally results in reduced order and consequently lowered charge mobilities, D-A dyads with a covalent link have recently been synthesized.[55–57] HBC derivatives with pyrene[55], anthraquinone,[56] or PMI[57] units have previously been investigated by scanning tunneling microscopy (STM) and X-ray diffraction revealing nanoscale phase segregation in monolayer and bulk systems.

Here, we demonstrate that a new D-A dyad composed of π-stackable HBC and PMI components can form highly ordered nanoscopic, mesoscopic, and macroscopic structures featuring nanoscale phase separation between D and A. In contrast with previous studies, the present work is focused on an HBC-PMI dyad equipped with an ethinylene bridging unit. The self-assembly of the HBC-PMI is explored across multiple length scales, revealing the formation of crystalline extruded filaments, uniform mesoscopic ribbons, networks of nanofibers, and ordered monolayers at the solution-graphite interface. In addition, electrical measurements in a transistor configuration show ambipolar characteristics and, compared with thin-film architectures, an improved mobility in the highly-ordered mesoscopic ribbons.

## 2. Synthesis and Bulk Characterization

### 2.1. Synthesis

The starting material consisted of the ethinyl substituted HBC derivative (Scheme 1), which has been previously prepared over 11 steps with an overall yield of about 4%.[58] This compound was coupled in a straight forward Hagihara-Sonogashira cross-coupling reaction with 9-bromo-N-(2,6-di-iso-propylphenyl)-perylene-3,4-dicarboxiimide (obtained from BASF).

After the column chromatographical purification, HBC-PMI (Scheme 1) was obtained in good yield. The purity was confirmed by the matrix-assisted laser desorption/ionization time of flight (MALDI-TOF) spectrum (see Supporting Information). The determined isotope distribution was in good agreement with the simulation. However, the spectrum showed traces of impurities which could not be assigned. Furthermore, NMR spectra could be recorded from the highly soluble, purple HBC-PMI. All proton resonances could be assigned to their corresponding nuclei (see Supporting Information) using two dimensional NMR experiments (HH COSY and NOESY). The $^1$H NMR spectrum did not reveal any impurities.

It should be noted that the synthesis of the HBC-PMI dyad with an ethinylene bridging unit can be produced in higher yields and with less side-products than similar dyads with a single-bond linkage. This is a result of the use of the Hagihara-Sonogashira protocol rather than a tedious purification step after the palladium catalyzed cross-coupling reaction. Moreover, the introduction of a carbon-carbon triple bond in between the HBC and PMI causes less steric problems than the formation of a single C-C bond between the building blocks. This is supported by density functional theory (DFT) calculations which show, as expected, a significantly reduced energy required for rotation in the ethinylene-bridged system, when compared with the single-bonded analogue.

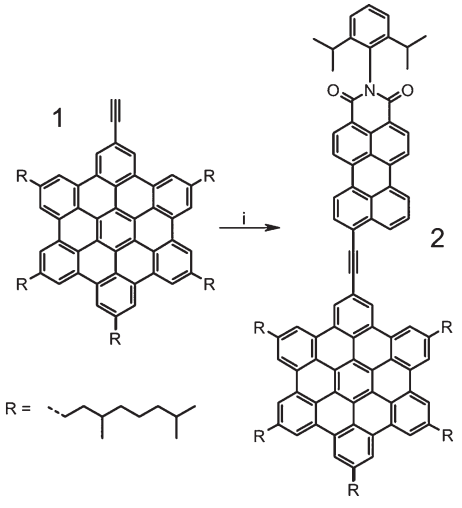


**Scheme 1.** Chemical formula of **1** ethinyl substituted HBC, **2** HBC-PMI. **i**: 9-Bromo-N-(2,6-di-iso-propylphenyl)-perylene-3,4-dicarboxiimide, $PPh_3$, CuI, $Pd(PPh_3)_4$, 72%.

### 2.2. Optical Characterization

The UV/vis spectrum of HBC-PMI in chloroform, shown in Figure 1, consisted of two distinct maxima: a structured UV absorption with a maximum at around 380 nm and the other more bathochromic with a maximum of 540 nm. These match the characteristic absorption bands for HBC and PMI, respectively.[59] Thus, it is clear that the UV absorption originates from the donor HBC and the blue absorption from the accepting PMI moiety. This

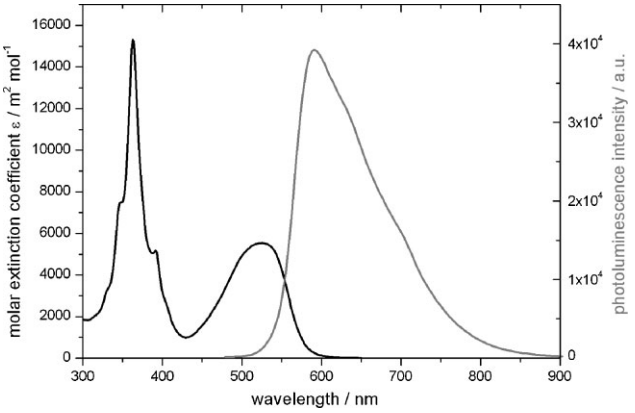


**Figure 1.** UV/vis and photoluminescence (excitation at 370 nm) spectrum of HBC-PMI recorded in chloroform.

suggests a weak electronic coupling within the dyad, which has also been observed for similar compounds.[60]

Excitation at 370 nm led to a strong, broad yellow photoluminescence which was shifted bathochromically by 50 nm compared to a PMI functionalized HBC derivative coupled by a single bond. This indicates a somewhat increased, but nevertheless weak coupling of the donor and the acceptor component in the ethinylene-bridged system. Investigation of the energy transfer between donor and acceptor revealed a process with an efficiency of more than 98%. Expectedly, the photoluminescence quantum efficiency (54%) was much higher than for unsubstituted HBC derivatives as a result of the presence of the rylene chromophore.

### 2.3. Thermotropic Organization

The thermal behavior was investigated by differential scanning calorimetry (DSC) (see Supporting Information). In the temperature range from −150 to 300 °C, one clear endothermic peak at 217 °C was found, which was assigned to a crystalline-liquid crystalline (LC) transition by means of two-dimensional wide-angle X-ray scattering (2D-WAXS). Compared to the parent HBC, HBC-$C_{8,2}$,[61] which carries six identical alkyl chains, the LC phase for HBC-PMI was reached at far higher temperatures, due to the extended π-area and therefore a stronger packing in the crystalline phase.

At a temperature of 240 °C, the 2D-WAXS pattern of a mechanically extruded HBC-PMI filament revealed a columnar hexagonal LC state with a lattice constant a = 3.0 nm, very similar to the size of the molecule (Fig. 2a). No higher order reflections could be observed, indicating the predominance of short-range correlations which are characteristic of such a mesophase. In the discotic LC phase, the molecular dynamics increase and the molecules start to rotate about their axis, as previously found by solid-state NMR for alkyl substituted HBCs,[62,63] leading to the above mentioned short-range order. In the case of HBC-PMI, the packing parameter of 3.0 nm represents a spacing between the mass centers of the whole molecules. In the columnar structures, the discs stack orthogonal to the columnar axis with a π-stacking distance of 0.35 nm, as derived from the high intensity meridional reflection in the wide-angle region.

The 2D-WAXS pattern changes significantly after cooling the sample to 30 °C (Fig. 2b) and shows a well-organized, crystalline material. The equatorial reflex distribution revealed an atypically large square unit cell with a lattice constant of $a = 5.31$ nm (Fig. 2c). The considerable increase of the unit cell is attributed to additional correlations taking place compared to the high temperature phase. Lowering the temperature decreases the molecular motion and results in correlations between individual HBC and PMI units. A series of meridional reflexes were found, which correspond to different stacking distances within the discotic material and suggest a high lateral order of the columns. This is in contrast to the case of HBC-PMI with a single bond link between the HBC and PMI, which did not exhibit long-range order.[57] Clearly, the presence of the triple bond, which reduces steric effects between the HBC and PMI, allows for increased intermolecular order.

Based on the 30 °C 2D-WAXS information, the supramolecular organization of the HBC-PMI molecules could be simulated

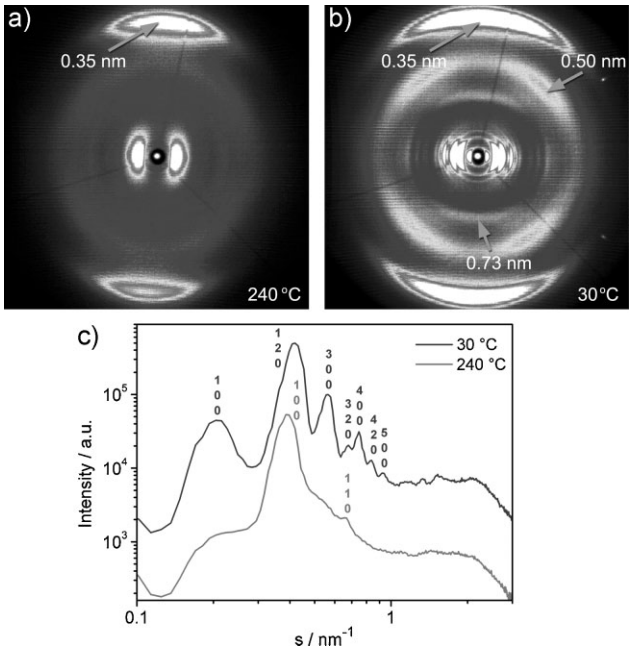


**Figure 2.** 2D-WAXS pattern of a mechanically extruded HBC-PMI filament a) recorded at 240 °C (hexagonal unit cell with $a = 3.0$ nm) and b) recorded at 30 °C (square unit cell with $a = 5.31$ nm). c) The equatorial scattering intensity distribution as a function of the scattering vector s at 240 °C and 30 °C. The peaks are labeled by their Miller indices according to the determined unit cell.

(Fig. 3). It is known that bulky units bring about large steric requirements in the core periphery which may induce a lateral rotation of the molecules around the columnar axis. In the present case, since the aromatic PMI unit is rotated out of plane with respect to the HBC core, as indicated by the off-meridional 2D-WAXS reflexes, two adjacent disks are not able to stack on top of each other with the same configuration, resulting in the lateral rotation of the molecules. Similar correlations between substituents in the core periphery resulting in such reflections were reported also for hexaphenyl HBCs.[64]

The meridional reflection peak corresponding to a real-space distance of 0.73 nm, related to every second disk, indicates that the

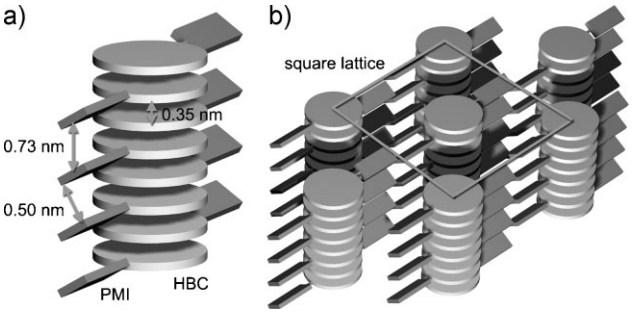


**Figure 3.** Schematic representation of a) the columnar stacks and b) the square lattice arrangement of stacks exhibited by HBC-PMI in the low temperature phase. HBC and PMI are represented by disks and rectangles, respectively. The intermolecular spacings fit the meridional reflections of the 2D-WAXS.

molecules adopt only two different arrangements in the stacks. This means that every second molecule within the column is oriented the same way. The off-meridional reflections can be explained by the calculated tilting of the perylene moieties with an angle of nearly 45°, which is also the azimuthal angle of the reflections. The rotation of the PMI unit is further supported by DFT calculations which show an equilibrium angle of 53° between the HBC and PMI units for isolated molecules, and a small energy required for rotation. The separation of 0.5 nm is in very good accordance with every second tilted perylene unit attached to the aromatic core. It should be noted, however, that the precise arrangement of the PMI units with respect to their neighbors, e.g. whether they face their neighbors with a parallel or perpendicular geometry, cannot be determined based on the X-ray results. Overall, the large aromatic HBC moieties dominate the stacking and form a non-tilted columnar superstructure. Interestingly, both the donating and accepting entities within the dyad form a nano-separated columnar superstructure.

## 3. Self-Assembly at Surfaces

### 3.1. Self-Assembly on Graphite at the Liquid-Solid Interface

Scanning tunneling microscope (STM) imaging of HBC-PMI at the interface between a saturated solution in 1-phenyloctane and the basal plane of highly oriented pyrolytic graphite (HOPG) revealed the formation of ordered and densely packed monolayers (Fig. 4a). The molecules self-assemble in a lamellar configuration, which upon careful inspection reveals brighter and darker rows, with two bright rows for each dark one. According to the resonance-enhanced tunneling model, the STM image contrast is mainly dependent on the energy difference between the frontier orbitals of the adsorbed molecule and the Fermi level of the substrate.[65] Based on DFT calculations, the difference between the highest-occupied molecular orbital (HOMO) of the HBC core and the graphite Fermi level is about 0.5 eV smaller than that for the PMI.

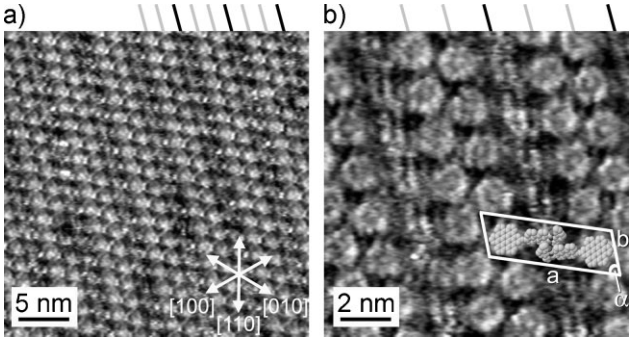


**Figure 4.** STM height images of HBC-PMI monolayers at the solution-graphite interface using 1-phenyloctane as the solvent: a) 30 nm × 30 nm, b) 12 nm × 12 nm. The principal crystallographic lattice directions of the graphite are indicated in (a). Sample bias voltage = −950 mV, average tunneling current = 2.5 pA for both images. The grey and black lines, shown at the top, point out the bright and dark contrast of the rows. The unit cell and proposed packing arrangement are shown in (b) (the alkyl chains are omitted for clarity).

Therefore, the brighter spots in Figure 4a can be ascribed to the HBC moieties, while the darker spots can be attributed to the PMI. Details of the packing arrangement are evident from high resolution images (Fig. 4b): the planar HBC discs lie flat on substrate, and located in between every second HBC row are the PMI units. The lamellar nanoscale phase segregation between D and A components is reminiscent of that observed in related HBC-PMI[57] and pyrene-substituted HBC systems.[55]

The unit cell, containing two molecules, was measured to have lattice constants $a = (5.32 \pm 0.13)$ nm, $b = (1.83 \pm 0.04)$ nm, and angle $\alpha = (64.8 \pm 1.4)^\circ$, with each molecule occupying an area of $(4.4 \pm 0.3)$ nm$^2$. The dimensions were corrected for drift by using the underlying HOPG lattice as a reference. The main axis of the unit cell is shorter than twice the length of the HBC-PMI molecule ($2 \times 3.36$ nm). This suggests an interdigitation of the PMI units (belonging to adjacent molecules) which are likely, due to steric effects, to be rotated out of plane. The length of the molecule was estimated by considering only the first three methylene units of the alkyl chains. This is because the packing of the remaining part of the chains, after the branching point, onto the surface is likely to be sterically hindered, leaving them extending into the solution.[55] This, in part, also explains why the alkyl chains surrounding the HBC cores are not well resolved. The portions of the alkyl chains which remain on the surface have a dark contrast, owing to their poor conductivity, and fill the interstices surrounding the HBC cores.

The out-of-plane rotation of the PMI units is further supported by considering the van der Waals area of the HBC-PMI dyad in a flat conformation and in a conformation where the HBC and PMI units are normal to one another. Again, considering only the first three methylene units in the alkyl chains, the area of the flat configuration is estimated to be 5.4 nm$^2$ while the footprint of the dyad with a rotated PMI unit is about 4.3 nm$^2$. The latter corresponds well with the measured area per molecule of $(4.4 \pm 0.3)$ nm$^2$. Additional evidence for a rotated PMI unit is provided by the relatively high tunneling impedance (>100 GΩ) required for imaging, which indicates an appreciably thick tunneling barrier. This result is in good agreement with the similarly high tunneling impedances previously required for imaging related PMI-HBC-PMI triads (with the moieties bridged by single C–C bonds) when the packing resulted in edge-on components; flat-lying configurations for the analogue HBC-PMI dyads called for much smaller impedances for imaging.[57] The edge-on packing of the PMI on HOPG is also likely to contribute to the less bright contrast exhibited by the PMI in the STM current images, relative to the HBC cores. Based on the STM measurements alone, it is not possible to determine the precise tilt angle of the PMI. It is expected that the neighboring tilted PMI units are arranged parallel to one another and stabilized by π-π stacking. This indicates that the energy gained by PMI-PMI π-π stacking is greater than the PMI-HOPG binding energy.

### 3.2. Self-Assembly of Nanofibers and Mesoscopic Ribbons

The HBC-PMI dyad was cast onto freshly cleaved mica and $SiO_2$ from different solvents by using spin-coating, drop-casting, and immersion methods. The surface morphology was measured by

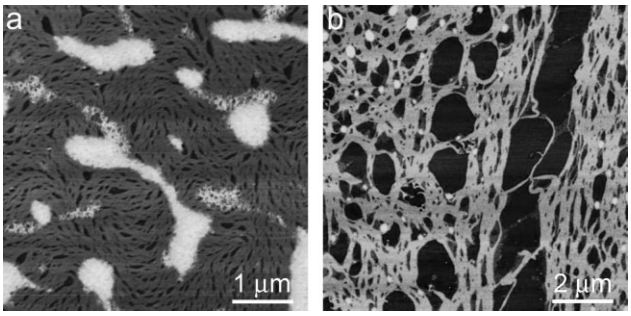


**Figure 5.** AFM topography images of HBC-PMI nanofiber networks obtained by spin-coating in a) chloroform (image 5 μm × 5 μm), and b) dichloromethane (image 10 μm × 10 μm).

atomic force microcopy (AFM) in the intermittent contact mode. The most significant results were obtained by spin-coating onto mica from chloroform and dichloromethane solutions, yielding networks of nanofibers (Fig. 5). The majority of the fibers had a height of (1.6 ± 0.2) nm, which closely matches the maximum molecular length of about 1.7 nm along the short-axis of the molecule (estimated as in the previous section by considering only the first three methylene units in the aliphatic side chains). This result suggests an edge-on arrangement of the HBC-PMI dyad, with the molecules forming π-stacks along the axis of the fibers. Some taller fibers with heights of (4.1 ± 0.2) nm were also observed, indicating the presence of two-layer structures. The interlayer separation of (2.5 ± 0.2) nm closely matches that measured by 2D-WAXS (2.66 nm) in macroscopic extruded fibers. The width of the nanofibers was measured to be as small as a few tens of nanometers. The spin-coated samples also exhibited some taller irregular features with variable height, signifying a reduced degree of internal order in these structures.

In an effort to improve the long-range order of the self-assembled surface structures, solvent vapor annealing (SVA)[49,54,66–69] was employed. This method involves exposing the sample to a solvent vapor, which promotes the mobility and reorganization of the surface absorbates. On gold substrates, following SVA treatment in a chloroform atmosphere at room temperature, mesoscopic ribbons with lengths ranging from tens of microns up to 150 microns were obtained (Fig. 6a–c). The ribbons had a mean width of 830 nm and a mean height of 250 nm, with the size distributions characterized by standard deviations of 280 nm and 160 nm, respectively. Scanning electron microscope (SEM) (Fig. 6b) and AFM (Fig. 6c) measurements revealed a flat, highly uniform structure. Moreover, high resolution AFM showed that the top of the ribbons were atomically flat, indicating crystalline facets and crystalline order within the mesoscopic structures. In some cases, molecular steps were observed, predominantly along the axis of the fibers. The steps were most apparent in the AFM phase channel (Fig. 6d), and possessed a height of (2.5 ± 0.3) nm (Fig. 6e). This height is in excellent agreement with the crystal unit cell determined by 2D-WAXS in mechanically extruded filaments where the face-centered square unit cell was determined to have an interlayer separation of 2.66 nm.

Similar ribbons were obtained following SVA treatment on $SiO_2$ substrates as well (not shown); however, the dimensions were

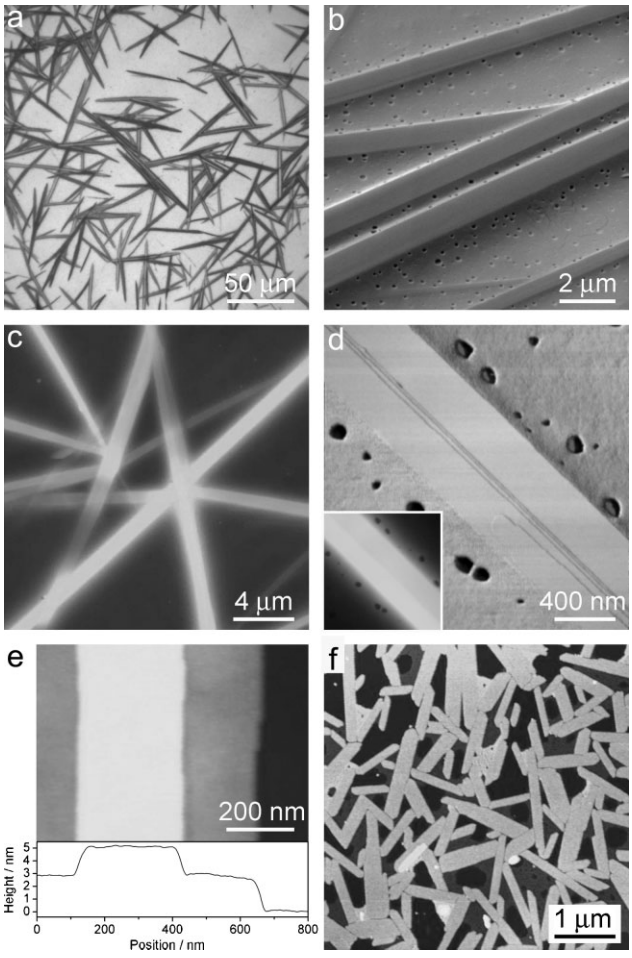


**Figure 6.** Mesoscopic HBC-PMI ribbons obtained after SVA treatment in chloroform vapor on a gold substrate. a) Optical microscope, b) SEM, and c) AFM topography images showing the uniform and flat shape of the ribbons. d) Phase channel AFM, with the corresponding topography in the inset and e) AFM topography, with a line profile at the bottom, showing single molecule steps on top of a ribbon. f) AFM topography image of HBC-PMI needles formed after SVA in chloroform vapor on a mica substrate. The holes in (b) and (d) are likely to be defects in the gold substrate.

generally smaller with lengths of less than 35 μm. On mica, the reorganization upon SVA treatment was even less pronounced, leading to flat sub-micron-scale needles (Fig. 6f). The mean length and widths of the needles were 750 nm and 150 nm, with standard deviations of 340 nm and 40 nm, respectively. The needles possessed a uniform height of (4.2 ± 0.1) nm with respect to the substrate. In some areas, a less ordered first layer was visible, with a height of (1.6 ± 0.1) nm, similar to the height of spin-coated first layer structures. The height of the needles above the first molecular layer was (2.6 ± 0.1) nm, which very closely matches the step height measured on top of mesoscopic ribbons and the interlayer spacing measured by 2D-WAXS in extruded macroscopic fibers.

The reduced reorganization of the HBC-PMI dyad on mica, and to a lesser degree $SiO_2$, compared to gold, reflects a reduced range of mass transport of the molecule on the substrate during SVA.

This can be understood on the basis of the relative polarity of the substrates (gold < $SiO_2$ < mica). Given that chloroform is a weakly polar solvent, it interacts most favorably with the apolar gold and least favorably with the polar mica surface. The affinity of halogens for gold is also likely to contribute to the increased interaction between chloroform and the gold surface. During SVA, a thin layer of solvent (a few tens of nanometers thick)[69] is condensed on the substrate which provides a medium for mass transport. The favorable wetting conditions between the gold and chloroform result in a uniform solvent layer suitable for long-range transport. Conversely, the chloroform has a reduced wetting on the more polar substrates, resulting in a reduced solvent layer and less molecular diffusion.

In addition to the solvent-substrate interaction, molecule-substrate interactions are also likely to play a role in determining the range of the mass transport process. More precisely, the heteroatoms in the PMI moiety may interact relatively strongly with polar surfaces, resulting in reduced molecular diffusion on the substrate. On the other hand, if the substrate is too apolar, the HBC unit may interact too strongly, as suggested by the result that HMDS-treated $SiO_2$, which renders the substrate highly hydrophobic, was not suitable for ribbon formation upon SVA treatment. This highlights the delicate balance involved between molecule-substrate interactions and the molecule-molecule interactions required for self-assembly. The interaction of the solvent with the molecule is also important, and generally should provide sufficient solubility to disassemble pre-existing surface structures, while still not competing too strongly with supramolecular interactions.[54]

Although the one-dimensional assembly of p- and n-type fibers has recently been demonstrated,[42,49,53,66,70] little prior work has been done on ordered supramolecular wires which combine p- and n-type components. Such fibers represent a new class of materials which combines the high degree of order present in single crystals with the ease of solution processing. The D and A units in the present ribbons provide additional functionality which makes the structures attractive for applications in electronic and optoelectronic devices such as OFETs, OLETs, and organic solar cells.

## 4. Electrical Properties

The extended π-π system presented by the highly ordered HBC-PMI stacks is expected to lead to charge delocalization and favorable charge transport characteristics. Moreover, the "coaxial" nano-separated superstructure consisting of donating and accepting entities provides the possibility for the simultaneous transport of holes through the HBC and electrons through the PMI.

Charge transport measurements were performed in a transistor configuration under ambient conditions. A bottom gold contact, bottom gate geometry was employed with either thin spin-coated films or SVA-prepared mesoscopic ribbons as the active layer. Hexamethyldisilazane (HMDS) was used to treat the $SiO_2$ substrates in order to improve the transport properties at the organic/$SiO_2$ interface.[71,72] The treatment was not used however for the ribbon-based devices, since the reduced substrate polarity interfered with the ribbon formation. No further means were employed in order to optimize the device configuration or composition. Further details about the device fabrication and characterization are provided in the Experimental Section.

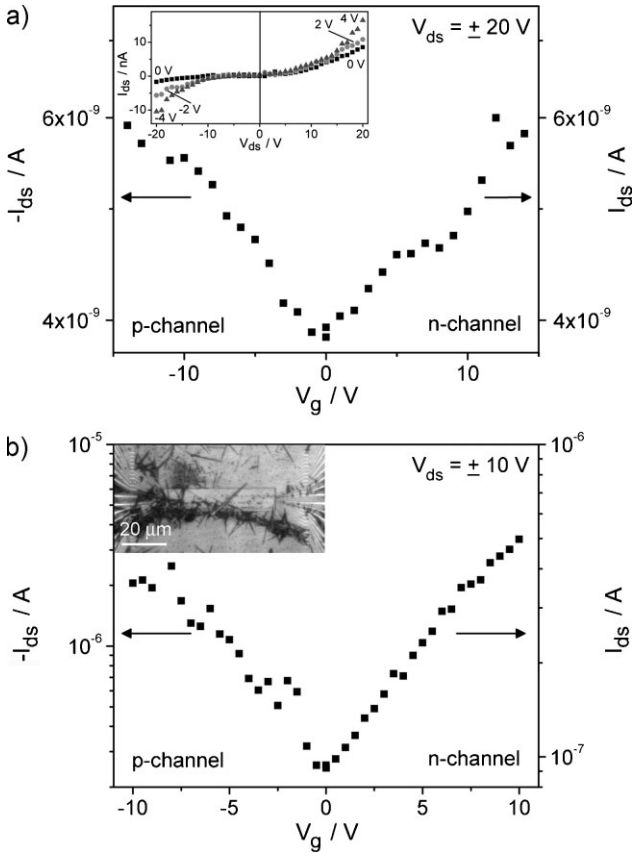


**Figure 7.** a) Transfer characteristics of an HBC-PMI thin film transistor (output characteristics in inset). b) Transfer characteristics for a transistor based on mesoscopic HBC-PMI ribbons. Inset: optical microscope image of HBC-PMI ribbon devices consisting of ribbons grown by SVA on top of an array of gold electrodes spaced 100 nm apart.

The transfer and output characteristics of an HBC-PMI thin film transistor are shown in Figure 7a. The devices exhibit an increase in source-drain current with both positive and negative gate voltages, which is indicative of ambipolar transport.[28–35] The linear regime electron and hole mobilities were both estimated to be $3 \times 10^{-6}$ $cm^2V^{-1}s^{-1}$. Such a balance between the electron and hole mobilities is desirable in ambipolar transistors, e.g., for CMOS device operation, and in OLETs, for maximizing exciton recombination. Devices with mesoscopic HBC-PMI ribbons as active components (Fig. 7b) had mobilities which were more than one order or magnitude higher, with estimated electron and hole mobilities of $7 \times 10^{-5}$ $cm^2V^{-1}s^{-1}$ and $1 \times 10^{-4}$ $cm^2V^{-1}s^{-1}$, respectively. It should be noted that the ribbons do not form a complete layer (see Fig. 7b inset) and that the corresponding mobilities, calculated assuming a complete coverage, represent lower limits. The improved mobility in the ribbons is likely to result from the improved supramolecular order in the ribbon structures. The obtained mobilities are comparable with those previously reported for ambipolar systems under ambient conditions,[32] albeit they are 1–2 orders of magnitude lower than those observed in optimized ambipolar devices under controlled environments.[29,30] The nonlinear output behavior at low drain-source voltages suggests sizeable charge injection barriers at the

interfaces. Moreover, it was not possible to operate the transistors in the saturation regime due to short-channel effects,[73,74] and instabilities at high voltages. It is expected that the performance can be significantly improved through optimization of the contact geometry, the electrode workfunctions, and the dielectric interface.[29,30,36,75–77] Degradation in device performance as a result of environmental instability is also likely to be a factor and can be avoided through the use of an inert atmosphere or vacuum conditions.[29,31]

The observation of ambipolar behavior is not unexpected given the p- and n-type nature of the HBC and PMI components of the molecule. Nevertheless, it is quite remarkable that n-type transport could be achieved given that n-channel operation in organic transistors is often elusive and that the present devices were not optimized. Generally, n-type behavior is thought to be inhibited by charge trapping at the dielectric interface, adverse humidity effects, and large injection barriers introduced by the typically used high workfunction electrode materials, such as gold.[29] Current flux could also be reduced by electron-hole recombination; however this pathway also offers an interesting opportunity for harvesting light, i.e., with the transistor operating as an organic light emitting transistor (OLETs).[33,36–38] Strategies to overcome the above problems include interface engineering,[29,75–77] and the use of source and drain electrodes with different work functions.[30,36] Blending[28] and heterostructure[30] approaches have also been employed to achieve ambipolar behavior, however the former can result in reduced molecular order and the latter requires orthogonal solvents for the fabrication. The present π-stackable D-A dyad represents a prototypical approach to combining p- and n-type transport channels in a single highly-ordered solution processable layer. These results are complementary to other recent work which shows ambipolar characteristics in amorphous D-A dyad films,[78] and D-A pairs held together by hydrogen-bonds.[79]

## 5. Conclusions

A new electron donor-acceptor (D-A) dyad based on HBC-PMI bridged through an ethinylene linker was synthesized and shown to form highly-ordered self assembled structures at multiple length scales ranging from macroscopic fibers to molecular monolayers. 2D-WAXS of extruded filaments revealed a crystalline packing with nanoseparated coaxial D-A regions and long-range order. Entangled networks of nanofibers were produced on surfaces by simple spin-coating, while highly-ordered ribbon structures were obtained by SVA treatment. The high degree of order in the latter structures was evidenced by the uniform linear appearance of the fibers, and the presence of atomically flat terraces on top with step heights corresponding to the interplane separation measured by 2D-WAXS in bulk samples. The dyad also formed ordered monolayers on the basal plane of HOPG, as measured by STM at the liquid-solid interface.

The obtained self-assembled π-stacked systems with nanoseparated coaxial D-A domains represent an interesting testbed for organic (opto)electronic applications. Initial electrical measurements in a transistor configuration were carried out, exhibiting ambipolar transport. In addition, owing to the high degree of supramolecular order, devices incorporating mesoscopic ribbons as the active material displayed improvements in p- and n-type mobilities of more than one order of magnitude. These measurements confirm that the general strategy of coupling D-A, π-stackable units to form D-A materials with nanoscale supramolecular order is viable and shows promise for producing organic devices such as ambipolar OFETs, OLETs, and organic solar cells.

## 6. Experimental

*Synthesis*: 9-[5,8,11,14,17-Penta(3,7-dimethyloctyl)-hexa-*peri*-hexabenzocoronen-2-yl]-N-(2,6-di-iso-propylphenyl)-perylene-3,4-dicarboxiimide (Scheme 1 molecule **2**) was synthesized as follows: 90 mg 9-Bromo-N-(2,6-di-iso-propylphenyl)-perylene-3,4-dicarboxiimide (160.3 μmol), 200 mg 2-acetyl-5,8,11,14,17-penta(3,7-dimethyloctyl)-hexa-*peri*-hexabenzocoronene (Scheme 1 molecule **1**, 160 μmol), 1.1 mg triphenylphosphine (4.2 μmol) and 11 mg copper(I) iodide (5.8 μmol) were dissolved in 10 mL piperidin and degassed with three freeze-vacuum-thaw cycles. Afterwards, 66 mg tetrakis-(triphenylphosphino)-palladium(0) (5.8 μmol) were added and the mixture was stirred at 80 °C for 24 hours. After having removed the solvent in vacuo, the residue was purified via repetitive column chromatography (silica gel, a) dichloromethane, $R_f = 0.3–0.6$; b) gradient acetone to acetone, toluene = 1:40, $R_f = 0.3–0.4$; c) toluene: ethyl acetate = 40:1, $R_f = 0.2–0.4$). The product was finally reprecipitated into methanol to afford 198 mg of the title compound as a red-violet solid (72%, 115 μmol). MS (MALDI-TOF): m/z (%) = 1727 (24%), 1728 (30%), 1729 (26%), 1730 (15%), 1731 (4%) (calc. for $C_{128}H_{143}NO_2 = 1727.57\ g\ mol^{-1}$, isotope pattern: 1726 (24%), 1727 (34%), 1728 (25%), 1729 (12%), 1730 (4%)). UV/vis ($CHCl_3$): λ/nm (ε/$m^2 \cdot mol^{-1}$) = 348 (751), 363 (1531), 392 (516), 526 (553). $^1$H NMR (500 MHz, $C_2D_2Cl_4$, 400 K): $\delta = 8.87$ (s, 2H, $H_a$), 8.81 (d, 1H, $^3J(H,H) = 8.92$ Hz, $H_r$), 8.66 (s, 2H, $H_b$), 8.63 (s, 2H, $H_c$), 8.62 (s, 2H, $H_d$), 8.59 (s, 2H, $H_e$), 8.58 (s, 2H, $H_f$), 8.54 (s, 2H, $H_p$), 8.5–8.4 (m, 5H, $H_t$, $H_u$, $H_v$, $H_w$, $H_x$), 8.11 (d, 1H, $^3J(H,H) = 6.76$ Hz, $H_s$), 7.83 (t, 1H, $^3J(H,H) = 8.44$ Hz, $H_q$), 7.44 (dt, 1H, $^3J(H,H) = 7.36$ Hz, $^4J(H,H) = 1.18$ Hz, $H_{ab}$), 7.30 (d, 2H, $^3J(H,H) = 7.70$ Hz, $H_{aa}$), 3.22 (m, 10H, $H_g$), 2.80 (sept., 2H, $^3J(H,H) = 6.91$ Hz, $H_z$), 2.12 (m, 5H, $H_{h^*}$(chiral)), 1.96 (m, 5H, $H_{h^*}$(chiral)), 1.81 (m, 5H, $H_i$), 1.60 (m, 10H, $H_k$), 1.56–1.20 (m, 52H, $H_j$, $H_l$, $H_n$, $H_o$, $H_y$), 0.92 (m, 30H, $H_m$). $^{13}$C NMR (125 MHz, $C_2D_2Cl_4$, 400 K): $\delta = 162.90$, 145.28, 144.36, 140.28, 140.13, 140.09, 136.41, 136.10, 133.89, 130.96, 130.89, 130.81, 131.26, 131.15, 130.21, 130.16, 129.80, 129.42, 129.24, 129.15, 129.07, 128.32, 127.48, 127.01, 126.28, 124.38, 123.62, 123.41, 123.31, 123.06, 122.51, 122.45, 122.28, 121.25, 121.09, 121.00, 120.88, 120.82, 120.78, 120.08, 119.91, 119.60, 119.26, 118.92, 98.97, 87.38, 38.79, 38.69, 36.74, 34.02, 33.99, 32.48, 28.50, 27.19, 24.09, 23.14, 21.84, 21.78, 19.12. DSC (°C): 217 (200). Elemental Analysis: 89.02% C, 8.39% H, 0.91% N (calc.: 88.99% C, 8.34% H, 0.81% N, 1.85% O)

*Quantum Chemical Calculation*: Quantum chemical calculations were carried out to determine energies and HOMO/ LUMO levels, using a density functional theory (DFT) approach. The structures were optimized on the B3LYP/6-31G* level and subsequently an energy calculation was performed using the same basis sets (Spartan 2004). In order to estimate the energy required for rotation, the equilibrium angle was changed from about 60° to 20° and the resulting energies were compared again using the same methods.

*Sample Preparation*: Mica (Pelco, grade V5), silicon with a 100 nm thermally grown oxide, and gold were used as substrates. The mica was freshly cleaved prior to use, thus exposing atomically flat terraces. Silicon oxide and gold substrates were cleaned by bathing in 60 °C acetone for 30 minutes, rinsing in acetone and ethanol, and treating with UV/ozone (Novascan PSD-UV). HBC-PMI solutions in chloroform and dichloromethane (0.1 mM) were cast onto the substrates by spin-coating at 500 RPM for 1 min. Solvent vapor annealing (SVA) was performed at room temperature by placing the samples into a closed container with a saturated atmosphere of chloroform vapor for 40 h.

*Bulk Characterization*: Solution UV/vis spectra were recorded at room temperature using a Perkin-Elmer Lambda 100 spectrophotometer. In order to eliminate aggregation phenomena in solution, spectra of samples of different concentrations ($10^{-6}$–$10^{-7}$ M) in chloroform (spectroscopic grade) were compared to give the properties for the monomeric species in solution. Solution photoluminescence (PL) spectra were recorded at room temperature on a SPEX-Fluorolog II (212) spectrometer. Spectra of samples of different concentrations in chloroform were compared to extracted aggregation behaviors. Quantum yields of selected compounds were calculated by comparing a known standard (three different concentrations). Differential scanning calorimetry (DSC) was measured on a Mettler DSC 30 with heating and cooling rates of 10 °C/min in the range from −150 °C until thermal decomposition. Two-dimensional wide-angle X-ray scattering (2D-WAXS) measurements of oriented filaments were conducted using a rotating anode (Rigaku 18 kW) X-ray beam (CuK$\alpha$, pinhole collimation, double graphite monochromator) and CCD camera. The patterns were recorded with vertical orientation of the filament axis and with the beam perpendicular to the filament.

*Scanning Probe Microscopy*: Scanning tunneling microscopy (STM) [80,81] measurements at the liquid-solid interface were performed in the constant current mode using a Nanoscope IIIa Multimode setup from Digital Instruments. A saturated solution in 1-phenyloctane was applied to the basal plane of a freshly cleaved HOPG substrate (Advanced Ceramics, ZYH grade). STM tips were cut from 0.25 mm Pt/Ir wire. Scanning Probe Image Processor (SPIP) version 2.0 (Image Metrology ApS, Lyngby, Denmark) was used to evaluate the average unit cell dimensions and correct for piezo drift by using the HOPG lattice as a reference. Atomic force microscopy (AFM) [82] measurements were performed in the intermittent contact (tapping) mode under ambient conditions using a Digital Instruments Dimension 3100 AFM with a Nanoscope IV controller. Standard silicon cantilevers were used (Veeco MPP-11100) with a nominal spring constant of 40 N/m, resonance frequency of 300 kHz and tip radius of 10 nm.

*Electrical Characterization*: Organic transistors were prepared by using a bottom-contact, bottom-gate geometry. The front-side of heavily-doped n-type silicon wafers was covered with a 50 nm oxide grown by dry thermal oxidation. Macroscopic gold contact pads were defined by optical lithography and a lift-off process. An array of 52 parallel gold nanoelectrodes with 100 nm gaps was prepared by e-beam lithography and lift-off. The gold (23 nm) was deposited by evaporation, with a titanium adhesion layer (7 nm). Prior to use, the substrates were bathed in 60 °C acetone for 30 min, rinsed in acetone and ethanol, and cleaned using UV/ozone treatment (Novascan PSD-UV). Some substrates were treated with hexamethyldisilazane (HMDS) by heating HMDS in a closed container to 120 °C and exposing the sample, placed in the same container, to the HMDS vapor for 1 hour. The HMDS-treated substrates were subsequently rinsed with acetone and ethanol after which the hydrophobicity of the substrate was verified under a flow of Millipore water. The HBC-PMI structures were prepared on the electrodes by spin-coating and SVA, as outlined previously. Electrical characterization was performed under ambient conditions using a Cascade Microtech M150 probe station with SUSS PH110 probe manipulators. A Toellner TOE 8841 power supply and a Keithley 6517A electrometer, interfaced with Labview software were employed for applying voltages and measuring currents.

## Acknowledgements

We thank Dr. E. Devaux for recording the SEM images and Dr. E. Orgiu for helpful discussions. This work was supported by the EU through the EC FP7 ONE-P large-scale project no. 212311, Marie Curie RTN THREADMILL (MRTN-CT-2006-036040) and EST-SUPER (MEST-CT-2004-008128), and by the International Center for Frontier Research in Chemistry (FRC, Strasbourg). Nanofabrication work was done at MC2 Nanofabrication Laboratory, Chalmers University of Technology, Göteborg, Sweden and was financed by the FP6-Research Infrastructures (ARI) program through Contract No: 026029 (MC2ACCESS). Supporting Information is available online from Wiley InterScience or from the author.

Received: March 3, 2009
Revised: May 11, 2009
Published online: June 18, 2009

[1] J. L. Brédas, J. P. Calbert, D. A. da Silva, J. Cornil, *Proc. Natl. Acad. Sci. USA* **2002**, *99*, 5804.
[2] F. Cacialli, J. S. Wilson, J. J. Michels, C. Daniel, C. Silva, R. H. Friend, N. Severin, P. Samorì, J. P. Rabe, M. J. O'Connell, P. N. Taylor, H. L. Anderson, *Nat. Mater.* **2002**, *1*, 160.
[3] F. Cacialli, P. Samorì, C. Silva, *Mater. Today* **2004**, *7*, 24.
[4] H. Sirringhaus, *Adv. Mater.* **2005**, *17*, 2411.
[5] W. Pisula, A. Menon, M. Stepputat, I. Lieberwirth, U. Kolb, A. Tracz, H. Sirringhaus, T. Pakula, K. Müllen, *Adv. Mater.* **2005**, *17*, 684.
[6] A. Facchetti, *Mater. Today* **2007**, *10*, 28.
[7] A. R. Murphy, J. M. J. Fréchet, *Chem. Rev.* **2007**, *107*, 1066.
[8] C. Reese, Z. N. Bao, *Mater. Today* **2007**, *10*, 20.
[9] V. Coropceanu, J. Cornil, D. A. da Silva, Y. Olivier, R. Silbey, J. L. Brédas, *Chem. Rev.* **2007**, *107*, 926.
[10] B. A. Jones, A. Facchetti, M. R. Wasielewski, T. J. Marks, *Adv. Funct. Mater.* **2008**, *18*, 1329.
[11] M. Mas-Torrent, C. Rovira, *Chem. Soc. Rev.* **2008**, *37*, 827.
[12] C. E. Finlayson, R. H. Friend, M. B. J. Otten, E. Schwartz, J. Cornelissen, R. L. M. Nolte, A. E. Rowan, P. Samorì, V. Palermo, A. Liscio, K. Peneva, K. Müllen, S. Trapani, D. Beljonne, *Adv. Funct. Mater.* **2008**, *18*, 3947.
[13] F. J. M. Hoeben, P. Jonkheijm, E. W. Meijer, A. P. H. J. Schenning, *Chem. Rev.* **2005**, *105*, 1491.
[14] P. Samorì, V. Francke, K. Müllen, J. P. Rabe, *Chem. Eur. J.* **1999**, *5*, 2312.
[15] C. W. Struijk, A. B. Sieval, J. E. J. Dakhorst, M. van Dijk, P. Kimkes, R. B. M. Koehorst, H. Donker, T. J. Schaafsma, S. J. Picken, A. M. van de Craats, J. M. Warman, H. Zuilhof, E. J. R. Sudholter, *J. Am. Chem. Soc.* **2000**, *122*, 11057.
[16] J. P. Hill, W. S. Jin, A. Kosaka, T. Fukushima, H. Ichihara, T. Shimomura, K. Ito, T. Hashizume, N. Ishii, T. Aida, *Science* **2004**, *304*, 1481.
[17] P. Leclère, M. Surin, P. Viville, R. Lazzaroni, A. F. M. Kilbinger, O. Henze, W. J. Feast, M. Cavallini, F. Biscarini, A. Schenning, E. W. Meijer, *Chem. Mater.* **2004**, *16*, 4452.
[18] A. Schenning, E. W. Meijer, *Chem. Commun.* **2005**, 3245.
[19] S. X. Xiao, M. Myers, Q. Miao, S. Sanaur, K. L. Pang, M. L. Steigerwald, C. Nuckolls, *Angew. Chem. Int. Ed.* **2005**, *44*, 7390.
[20] Y. Yamamoto, T. Fukushima, Y. Suna, N. Ishii, A. Saeki, S. Seki, S. Tagawa, M. Taniguchi, T. Kawai, T. Aida, *Science* **2006**, *314*, 1761.
[21] J. S. Wu, W. Pisula, K. Müllen, *Chem. Rev.* **2007**, *107*, 718.
[22] S. Sergeyev, W. Pisula, Y. H. Geerts, *Chem. Soc. Rev.* **2007**, *36*, 1902.
[23] D. Gust, T. A. Moore, A. L. Moore, *Acc. Chem. Res.* **2001**, *34*, 40.
[24] J. J. M. Halls, C. A. Walsh, N. C. Greenham, E. A. Marseglia, R. H. Friend, S. C. Moratti, A. B. Holmes, *Nature* **1995**, *376*, 498.
[25] G. Yu, J. Gao, J. C. Hummelen, F. Wudl, A. J. Heeger, *Science* **1995**, *270*, 1789.
[26] L. Schmidt-Mende, A. Fechtenkötter, K. Müllen, E. Moons, R. H. Friend, J. D. MacKenzie, *Science* **2001**, *293*, 1119.
[27] H. Hoppe, N. S. Sariciftci, *J. Mater. Res.* **2004**, *19*, 1924.
[28] E. J. Meijer, D. M. De Leeuw, S. Setayesh, E. Van Veenendaal, B. H. Huisman, P. W. M. Blom, J. C. Hummelen, U. Scherf, T. M. Klapwijk, *Nat. Mater.* **2003**, *2*, 678.
[29] L. L. Chua, J. Zaumseil, J. F. Chang, E. C. W. Ou, P. K. H. Ho, H. Sirringhaus, R. H. Friend, *Nature* **2005**, *434*, 194.
[30] C. Rost, D. J. Gundlach, S. Karg, W. Riess, *J. Appl. Phys.* **2004**, *95*, 5782.
[31] T. D. Anthopoulos, C. Tanase, S. Setayesh, E. J. Meijer, J. C. Hummelen, P. W. M. Blom, D. M. de Leeuw, *Adv. Mater.* **2004**, *16*, 2174.
[32] T. D. Anthopoulos, S. Setayesh, E. Smits, M. Colle, E. Cantatore, B. de Boer, P. W. M. Blom, D. M. de Leeuw, *Adv. Mater.* **2006**, *18*, 1900.
[33] J. Zaumseil, H. Sirringhaus, *Chem. Rev.* **2007**, *107*, 1296.

[34] J. Cornil, J. L. Bredas, J. Zaumseil, H. Sirringhaus, *Adv. Mater.* **2007**, *19*, 1791.
[35] H. N. Tsao, W. Pisula, Z. H. Liu, W. Osikowicz, W. R. Salaneck, K. Müllen, *Adv. Mater.* **2008**, *20*, 2715.
[36] J. Zaumseil, R. H. Friend, H. Sirringhaus, *Nat. Mater.* **2006**, *5*, 69.
[37] M. Muccini, *Nat. Mater.* **2006**, *5*, 605.
[38] F. Cicoira, C. Santato, *Adv. Funct. Mater.* **2007**, *17*, 3421.
[39] B. Crone, A. Dodabalapur, Y. Y. Lin, R. W. Filas, Z. Bao, A. LaDuca, R. Sarpeshkar, H. E. Katz, W. Li, *Nature* **2000**, *403*, 521.
[40] T. D. Anthopoulos, D. M. de Leeuw, E. Cantatore, S. Setayesh, E. J. Meijer, C. Tanase, J. C. Hummelen, P. W. M. Blom, *Appl. Phys. Lett.* **2004**, *85*, 4205.
[41] A. M. van de Craats, J. M. Warman, A. Fechtenkotter, J. D. Brand, M. A. Harbison, K. Müllen, *Adv. Mater.* **1999**, *11*, 1469.
[42] M. Kastler, W. Pisula, D. Wasserfallen, T. Pakula, K. Müllen, *J. Am. Chem. Soc.* **2005**, *127*, 4286.
[43] K. Müllen, J. P. Rabe, *Acc. Chem. Res.* **2008**, *41*, 511.
[44] P. R. L. Malenfant, C. D. Dimitrakopoulos, J. D. Gelorme, L. L. Kosbar, T. O. Graham, A. Curioni, W. Andreoni, *Appl. Phys. Lett.* **2002**, *80*, 2517.
[45] F. Würthner, *Chem. Commun.* **2004**, 1564.
[46] R. J. Chesterfield, J. C. McKeen, C. R. Newman, P. C. Ewbank, D. A. da Silva, J. L. Brédas, L. L. Miller, K. R. Mann, C. D. Frisbie, *J. Phys. Chem. B* **2004**, *108*, 19281.
[47] M. Cotlet, S. Masuo, G. B. Luo, J. Hofkens, M. Van der Auweraer, J. Verhoeven, K. Müllen, X. L. S. Xie, F. De Schryver, *Proc. Natl. Acad. Sci. USA* **2004**, *101*, 14343.
[48] F. C. De Schryver, T. Vosch, M. Cotlet, M. Van der Auweraer, K. Müllen, J. Hofkens, *Acc. Chem. Res.* **2005**, *38*, 514.
[49] A. Datar, R. Oitker, L. Zang, *Chem. Commun.* **2006**, 1649.
[50] J. Elemans, R. Van Hameren, R. J. M. Nolte, A. E. Rowan, *Adv. Mater.* **2006**, *18*, 1251.
[51] K. Balakrishnan, A. Datar, T. Naddo, J. Huang, R. Oitker, M. Yen, J. Zhao, L. Zang, *J. Am. Chem. Soc.* **2006**, *128*, 7390.
[52] V. Palermo, A. Liscio, D. Gentilini, F. Nolde, K. Müllen, P. Samorì, *Small* **2006**, *3*, 161.
[53] A. L. Briseno, S. C. B. Mannsfeld, C. Reese, J. M. Hancock, Y. Xiong, S. A. Jenekhe, Z. Bao, Y. Xia, *Nano Lett.* **2007**, *7*, 2847.
[54] G. De Luca, A. Liscio, P. Maccagnani, F. Nolde, V. Palermo, K. Müllen, P. Samorì, *Adv. Funct. Mater.* **2007**, *17*, 3791.
[55] N. Tchebotareva, X. M. Yin, M. D. Watson, P. Samorì, J. P. Rabe, K. Müllen, *J. Am. Chem. Soc.* **2003**, *125*, 9734.
[56] P. Samorì, X. M. Yin, N. Tchebotareva, Z. H. Wang, T. Pakula, F. Jackel, M. D. Watson, A. Venturini, K. Müllen, J. P. Rabe, *J. Am. Chem. Soc.* **2004**, *126*, 3567.
[57] P. Samorì, A. Fechtenkötter, E. Reuther, M. D. Watson, N. Severin, K. Müllen, J. P. Rabe, *Adv. Mater.* **2006**, *18*, 1317.
[58] M. Kastler, Johannes Gutenberg Universität, Private communication **2002**.
[59] J. S. Wu, J. Q. Qu, N. Tchebotareva, K. Müllen, *Tetrahedron Letters* **2005**, *46*, 1565.
[60] A. Fechtenkötter, Johannes Gutenberg Universität, Private communication **2001**.
[61] A. Fechtenkötter, N. Tchebotareva, M. Watson, K. Müllen, *Tetrahedron* **2001**, *57*, 3769.
[62] I. Fischbach, T. Pakula, P. Minkin, A. Fechtenkötter, K. Müllen, H. W. Spiess, K. Saalwächter, *J. Phys. Chem. B* **2002**, *106*, 6408.
[63] W. Pisula, M. Kastler, D. Wasserfallen, M. Mondeshki, J. Piris, I. Schnell, K. Müllen, *Chem. Mater.* **2006**, *18*, 3634.
[64] W. Pisula, Ž. Tomović, M. D. Watson, K. Müllen, J. Kussmann, C. Ochsenfeld, T. Metzroth, J. Gauss, *J. Phys. Chem. B* **2007**, *111*, 7481.
[65] R. Lazzaroni, A. Calderone, J. L. Brédas, J. P. Rabe, *J. Chem. Phys.* **1997**, *107*, 99.
[66] G. De Luca, A. Liscio, F. Nolde, L. Monsù Scolaro, V. Palermo, K. Müllen, P. Samorì, *Soft Matter* **2008**, *4*, 2064.
[67] K. C. Dickey, J. E. Anthony, Y. L. Loo, *Adv. Mater.* **2006**, *18*, 1721.
[68] W. H. Lee, D. H. Kim, J. H. Cho, Y. Jang, J. A. Lim, D. Kwak, K. Choa, *Appl. Phys. Lett.* **2007**, *91*.
[69] E. Treossi, A. Liscio, X. L. Feng, V. Palermo, K. Müllen, P. Samorì, *Small* **2009**, *5*, 112.
[70] A. Liscio, V. Palermo, P. Samorì, *Adv. Funct. Mater.* **2008**, *18*, 907.
[71] H. Sirringhaus, N. Tessler, R. H. Friend, *Synth. Met.* **1999**, *102*, 857.
[72] M. H. Yoon, C. Kim, A. Facchetti, T. J. Marks, *J. Am. Chem. Soc.* **2006**, *128*, 12851.
[73] S. Sze, *Physics of Semiconductor Devices*, Wiley, New York **1969**.
[74] L. Torsi, A. Dodabalapur, H. E. Katz, *Journal of Applied Physics* **1995**, *78*, 1088.
[75] J. Veres, S. Ogier, G. Lloyd, D. de Leeuw, *Chem. Mater.* **2004**, *16*, 4543.
[76] A. Facchetti, M. H. Yoon, T. J. Marks, *Adv. Mater.* **2005**, *17*, 1705.
[77] Y. D. Park, J. A. Lim, H. S. Lee, K. Cho, *Mater. Today* **2007**, *10*, 46.
[78] T. P. I. Saragi, K. Onken, I. Suske, T. Fuhrmann-Lieker, J. Salbeck, *Opt. Mater.* **2007**, *29*, 1332.
[79] P. Jonkheijm, N. Stutzmann, Z. J. Chen, D. M. de Leeuw, E. W. Meijer, A. P. H. J. Schenning, F. Würthner, *J. Am. Chem. Soc.* **2006**, *128*, 9535.
[80] S. De Feyter, F. C. De Schryver, *J. Phys. Chem. B* **2005**, *109*, 4290.
[81] M. Surin, P. Samorì, *Small* **2007**, *3*, 190.
[82] P. Samorì, M. Surin, V. Palermo, R. Lazzaroni, P. Leclère, *Physical Chemistry Chemical Physics* **2006**, *8*, 3927.